Geophysical Research Letters

RESEARCH LETTER
10.1029/2019GL086856

# Lateral Variations of Shear-Wave Velocity in the D″ Layer Beneath the Indian-Eurasian Plate Collision Zone

**Guohui Li[1,2], Ling Bai[1], and Jeroen Ritsema[3]**

[1]Key Laboratory of Continental Collision and Plateau Uplift, Institute of Tibetan Plateau Research, Center for Excellence in Tibetan Plateau Earth Sciences, Chinese Academy of Sciences, Beijing, China, [2]Institute of Earthquake Forecasting, China Earthquake Administration, Beijing, China, [3]Department of Earth and Environmental Sciences, University of Michigan, Ann Arbor, MI, USA

**Abstract** Seismic tomography has demonstrated that the shear-wave velocity is relatively high over a 3,000-km wide region in the lowermost mantle beneath southern and eastern Asia. This seismic anomaly demarcates the current position of slab remnants that may have subducted in the Cretaceous. To further characterize the seismic structure at smaller scales, we measure 929 residual travel time differences ($\delta t$) between the phases *ScS* and *S* using recordings of eight earthquakes beneath the Indian Ocean at stations from the Chinese Digital Seismic Network. We interpret variations of $\delta t$ up to 10 s as due to horizontal shear-velocity variations in D″ beneath northern India, Nepal, and southwestern China. The shear velocity can vary by as much as 7% over distances shorter than 300 km. Our observations provide additional observational evidence that compositional heterogeneity and possibly melt contribute to the seismic structure of the lower mantle characterized by long-term subduction and mantle downwelling.

**Plain Language Summary** Seismic tomography indicates that the seismic wave speed is relatively high in the lowermost mantle (i.e., the D″ region) beneath regions, such as eastern Asia, influenced by subduction since the Mesozoic era. Our new analysis of the propagation time of shear-wave reflections off the outer core (i.e., the phase *ScS*) corroborates the result from seismic tomography that the shear velocity in D″ beneath eastern Asia is high overall. However, we also find that the shear velocity can vary by as much as 7% over distances shorter than 300 km within a region of D″ beneath northern India, Nepal, and southwestern China. This provides new evidence for the thermochemical nature of D″ beneath downwelling regions of the mantle.

**Key Points:**
- Using waveforms of *S* and *ScS*, we estimate the shear-wave velocity (*Vs*) structure in D″ beneath the Indian-Eurasian plate collision zone
- *Vs* is relatively high overall but we resolve horizontal variations by 3–7% over distances shorter than about 300 km
- Our models place new constraints on geodynamic scenarios for the generation of thermochemical heterogeneity in downwelling regions of D″

**Supporting Information:**
- Supporting Information S1
- Table S1

**Correspondence to:**
L. Bai,
bailing@itpcas.ac.cn

**Citation:**
Li, G., Bai, L., & Ritsema, J. (2020). Lateral variations of shear-wave velocity in the D″ layer beneath the Indian-Eurasian plate collision zone. *Geophysical Research Letters*, *47*, e2019GL086856. https://doi.org/10.1029/2019GL086856

Received 30 DEC 2019
Accepted 2 MAR 2020
Accepted article online 12 MAR 2020



## 1. Introduction

Seismic tomography models agree that the *P* wave and *S* wave velocities (*Vp* and *Vs*, respectively) are relatively high across a wide region of the lowermost mantle beneath eastern and southern Asia (e.g., Houser et al., 2008; Kustowski et al., 2008; Ritsema et al., 2011; Simmons et al., 2010) (Figure 1a). This broad seismic anomaly is the deepest portion of an elongated high-velocity anomaly from southeastern Asia to the Mediterranean at shallower depths in the lower mantle. Reconstruction of paleo-plates linked it to the subduction of the Neo-Tethyan and Pacific plates and the Paleo-Tethyan and Paleo-Pacific plates (e.g., Honza & Fujioka, 2004; Muller & Seton, 2015; Ricard et al., 1993; Stampfli & Borel, 2002; Van der Voo et al., 1999). Thus, the high seismic velocities in D″ beneath eastern and southern Asia are likely related to prolonged subduction in the region and relatively cool fragments of subducted material.

However, seismic tomography and various analyses of teleseismic body waves indicate that *Vp* and *Vs* vary also at smaller spatial scales. Studies of teleseismic *S* wave triplication (e.g., Young & Lay, 1987; Weber & Davis, 1990; Gaherty & Lay, 1992) showed that *Vs* increases discontinuously by about 2.8% at 280 km above the core-mantle boundary (CMB) beneath the Indian Ocean and eastern Eurasia. The waveform complexity suggest that the strength and depth of the discontinuity varies considerably. The discontinuity may be related to the phase transition of perovskite to postperovskite within a relatively cool lower mantle (e.g., Grocholski et al., 2012; Murakami et al., 2004). Within the wider D″ region of southeastern Asia, there is evidence for anisotropy in *Vs* (e.g., Ritsema, 2000; Thomas et al., 2007), weak scattering producing *PcP* precursors (Zhang et al., 2019), albeit not for ultralow velocity zones at the base of the mantle unless they are thinner than the detection thickness of about 5 km thick (Thorne & Garnero, 2004).

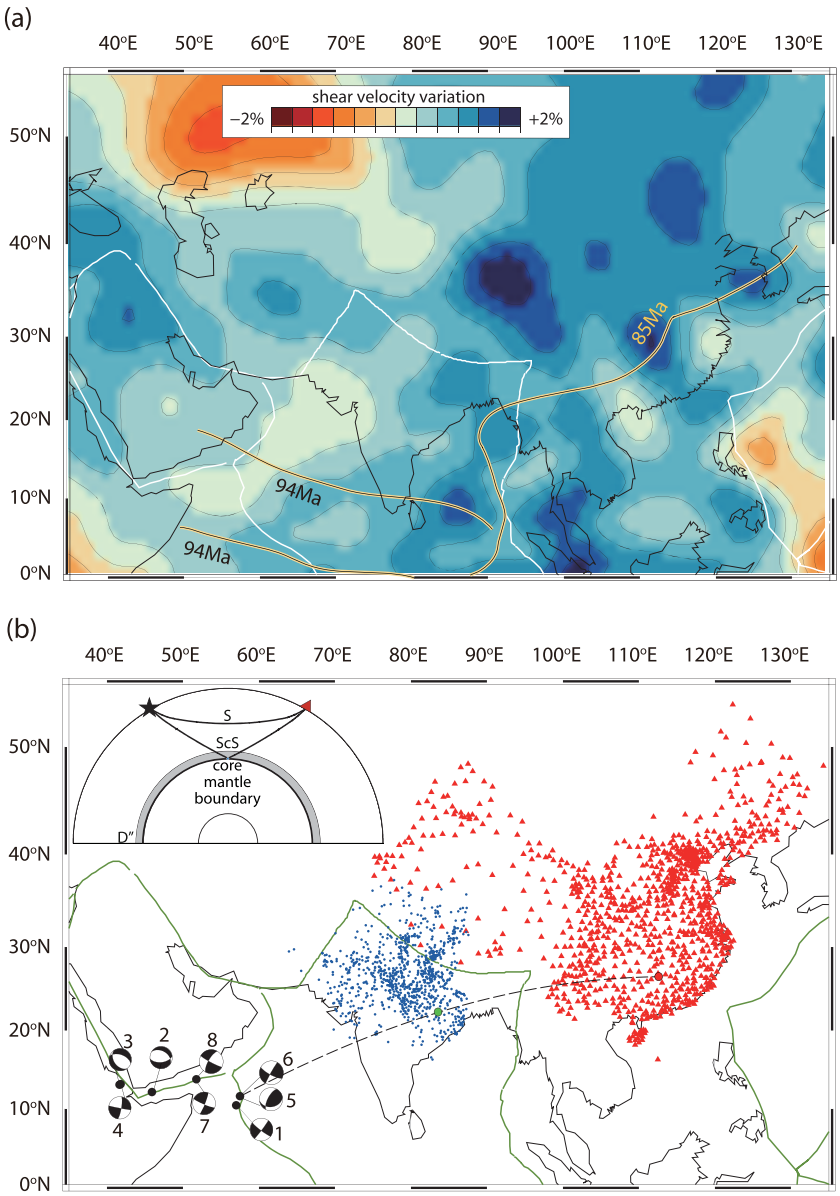


**Figure 1.** (a) Map of the variation of shear velocity in the lowermost mantle beneath southern Asia according to model S40RTS (Ritsema et al., 2011). The thick line from the eastern Indian Ocean to Korea is the plate boundary between the Pacific and Eurasian plates during the late Cretaceous to the late Eocene (Honza & Fujioka, 2004). Two east-west oriented thick lines beneath the Arabian Sea and the western Indian Ocean are the boundaries of Neo-Tethys Ocean and Eurasian plates during the late Cretaceous (Van der Voo et al., 1999). White lines denote current plate boundaries. (b) Map showing the locations of the eight earthquakes (black circles for the locations; beach balls for the focal mechanisms) and CDSN stations (red triangles) used in this study. The blue circles are the reflection points of 929 *ScS* phases. Green lines are the present plate boundaries. The dashed line marks the great-circle arc between Event 6 and station HN.CNS. The inset in the upper-left corner shows the *S* and *ScS* rays for an epicentral distance of 60°.

Detailed seismic mapping of D″ beneath Eurasia and other downwelling region is necessary to further evaluate the composition, mineralogy, and structural complexity of the ancient slabs that have accumulated above the CMB. We contribute to such work a study of the arrival-time differences of the phases *S* and *ScS* recorded by a network of more than thousand seismic stations in China (Figure 1b). Our unique data enable us to chart 100-km-scale variations of *Vs* within a 2,000 × 2,000 km$^2$ zone of D″ beneath northern India, Nepal, and southwestern China near the plate boundary of the Neo-Tethys slab.

## 2. *ScS-S* Differential Travel Time Residuals

### 2.1. Recorded and Synthetic Waveforms

The *ScS*-S difference time is a robust seismic observable and often used to study the seismic structure of the deep mantle. It is less strongly influenced by seismic structure in the upper mantle and by earthquake mislocations than the absolute travel times (e.g., He et al., 2015; Russell et al., 1998; Wysession et al., 2001; Zhao et al., 2017). We measure the arrival times of *ScS* and *S* by cross-correlating the band-pass filtered recorded and computed waveforms to account for all propagation effects on the *S* and *ScS* waveforms.

We use *ScS* and *S* waveforms recorded by the 1,024 stations from the Chinese Digital Seismic Network (CDSN) (Zheng et al., 2009). The waveform data were produced by eight shallow earthquakes with $M_W > 5.6$ between 2009 (when the deployment of the CDSN began) and 2018 along the Owen Fracture Zone and beneath the Red Sea (Table S1 and Figure 1b). We determine their focal depths and source mechanisms by modeling the interference of the direct *P* wave with the *pP* and *sP* surface reflections (e.g., Bai et al., 2017; Kikuchi & Kanamori, 1986) (Figure S1 in the supporting information) at stations not used in the study of *S* and *ScS*. The waveforms have been corrected for the effects of the instrument response.

We calculate synthetic waveforms using the spectral-element method (Komatitsch & Tromp, 2002). The cross-correlation window has a width of 16 s corresponding to the dominant period of the *ScS* and *S* waveforms. The cross-correlation function does not change significantly if the time window is up to a factor of two wider (Figure S2). With resources available to us, we can only compute synthetic waveforms with periods longer than 10 s. We apply therefore a second-order Butterworth filter with corner frequencies of 0.02 and 0.1 Hz (i.e., periods of 10–50 s). A filter of 10–50 s results in the sharpest *ScS* and *S* pulses and the best imaging results of shear-velocity variations in D″ (Figure S3). We select waveforms in which the *S* and *ScS* signals have signal to noise ratios (defined as the square root of the energy ratio of signal to noise) higher than 2.0 and manually checked each waveform to ensure the high quality of data. After these quality checks, we retain 929 transverse-component waveforms for epicentral distances between 46° and 77°.

We retain measurements only if the cross-correlation function has a maximum higher than 0.85 (Figure S4). To quantify the residuals, we consider a 1-D and a 3-D reference model. The reference 1-D profile is AK135 (Kennett et al., 1995). In the reference 3-D model, S40RTS (Ritsema et al., 2011) is the *Vs* structure in the mantle to a depth of 2,591 km and *Vs* follows the 1-D AK135 profile between 2,591-km depth and the CMB. Figure S5 compares S40RTS to nine other tomographic models.

### 2.2. Measurements

We write the travel time differences between the *S* wave and the *ScS* wave in the recorded waveform and synthetic waveform for the reference 1-D profile as $\Delta S^{1D}$ and as $\Delta ScS^{1D}$, respectively. The residual $\delta t^{1D} = \Delta ScS^{1D} - \Delta S^{1D}$ is the anomaly in the *ScS* and *S* arrival time difference with respect to AK135. Similarly, $\Delta S^{3D}$, $\Delta ScS^{3D}$, and $\delta t^{3D}$ denote anomalies in the arrival times of *S*, *ScS*, and the *ScS*-S arrival time difference with respect to the 3-D reference model.

Using two examples, we illustrate that the measurements of $\Delta S^{1D}$, $\Delta ScS^{1D}$, $\Delta S^{3D}$, and $\Delta ScS^{3D}$ can be significantly different for the two reference models. Figure 2a shows measurements and recorded and synthetic waveforms for Event 4 at station HB.JME at an epicentral distance of 66.7°. The *S*-wave arrival time is predicted within 1.5 s by either reference model but *ScS* arrives anomalously early by 3.9 s for the 1-D reference models and 5.5 s for the 3-D reference model. The values for $\delta t^{1D}$ and $\delta t^{3D}$ are −2.4 s and −5.9 s, respectively. This demonstrates that the *Vs* structure of the mantle above D″ has a significant influence on the *ScS* arrival time in particular. In addition, the 3-D waveform of *ScS* reproduces the "down-and-up" swing in the recorded *ScS* waveform better than the 1-D model.

Figure 2b shows the waveforms and modeling results for Event 6 recorded at station HN.CNS at an epicentral distance of 54.0°. The arrival time anomalies of both *S* and *ScS* differ by more than 5 s for the 1-D and 3-D reference models. However, $\delta t^{1D}$ and $\delta t^{3D}$ are similar at +4.8 and +4.1 s, respectively. This indicates that the *ScS*-S arrival-time difference is determined primarily by structure in D″.

The values for $\delta t^{3D}$ for HB.JME (Figure 2a) and HN.CNS (Figure 2b) are extreme values in our collection. The *ScS* reflection points associated with these two waveforms are [31.7°N, 72.9°E] and [22.3°N, 83.7°E], respectively. If S40RTS is indeed effective in removing the contributions of the mantle above D″ to the

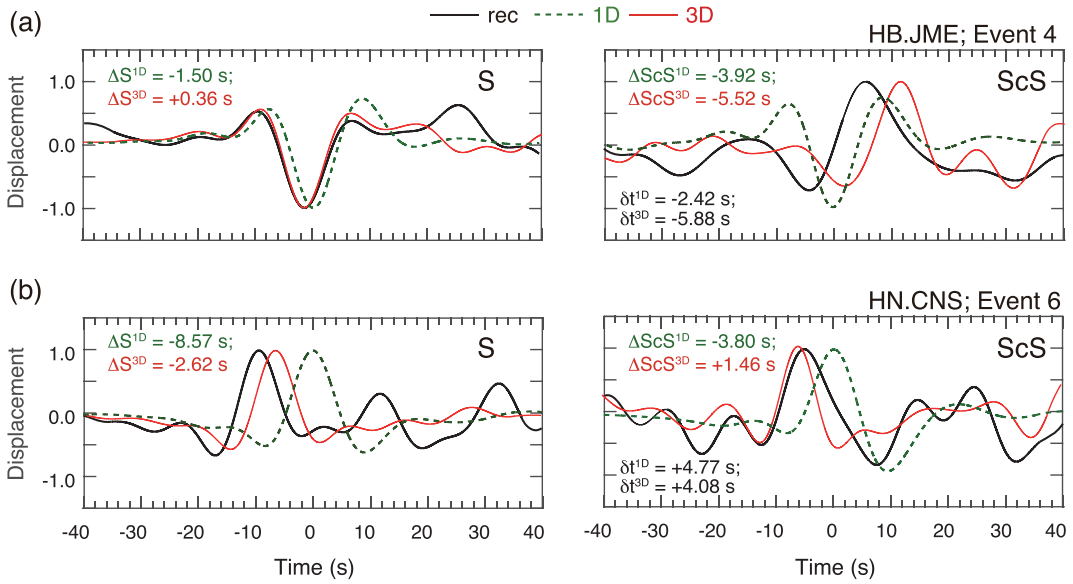


**Figure 2.** Example of measurements of $\Delta S^{1D}$, $\Delta ScS^{1D}$, $\Delta S^{3D}$, and $\Delta ScS^{3D}$, indicated in the upper left corners, at stations (a) HB.JME for Event 4 and (b) HN.CNS for Event 6. The recorded waveform segments are shown with black lines. The synthetics for the 1D and 3D reference models are shown using dashed green and red lines, respectively. The waveforms are 80 s long and have been centered on the AK135 predicted arrival time (at 0 s) of *S* (on the left) and *ScS* (on the right). The waveforms have been normalized so their maximum amplitudes are 1.

*ScS*-S arrival time difference, the 10-s variation of $\delta t^{3D}$ for HB.JME and HN.CNS points to a 6% difference in the average *Vs* velocity in D″ over 800 km.

Figure 3 shows the correlations of $\Delta S^{1D}$, $\Delta S^{3D}$, $\Delta ScS^{1D}$, $\Delta ScS^{3D}$, $\delta t^{1D}$, and $\delta t^{3D}$ for our 929 high-quality measurements. It demonstrates that the anomaly in the *ScS*-S arrival time difference (i.e., $\delta t^{1D}$ and $\delta t^{3D}$) correlates better with the anomaly in the *ScS* arrival time (i.e., $\Delta ScS^{1D}$ and $\Delta ScS^{3D}$) (Figures 3b and 3d) than the anomaly in the *S* arrival time (i.e., $\Delta S^{1D}$ and $\Delta S^{3D}$) (Figures 3a and 3c). Further, $\Delta ScS^{3D}$ correlates better with $\delta t^{3D}$ than $\Delta ScS^{1D}$ with $\delta t^{1D}$, which suggest that using a 3-D reference model is essential in isolating the *Vs* structure in D″ from the *ScS*-S arrival time measurements.

## 3. Modeling

The median value of the 929 measurements of $\delta t^{3D}$ is −1.75 s (Figure 4a). The predominantly negative values (84% of the total data set) indicates that *Vs* in the D″ is higher than the AK135 value (and other reference seismic profiles), consistent with the high-velocity anomalies imaged by seismic tomography (e.g., Figure 1a); 95% of all values of $\delta t^{3D}$ fall between −4.57 s and +1.63 s, indicating that *Vs* varies significantly in the *ScS* reflection point region. Part of this signal is an epicentral distance effect; the absolute value of $\delta t^{3D}$ increases with increasing epicentral distance (Figure S2) because *ScS* propagates a longer distance through D″.

Since *ScS* propagates steeply through D″, especially for the shortest epicentral distances, we cannot determine the thickness of D″ and the *Vs* structure in D″ independently from measurements of $\delta t^{3D}$. Therefore, similar to previous studies (e.g., Garnero & Lay, 2003; He & Wen, 2011), we assume that D″ has a uniform thickness, which is 300 km in our case, and adopt a tomographic model, S40RTS in our case, to describe the *Vs* variation in the mantle above D″. We relate a travel time anomaly $\delta t^{3D}$ to a perturbation in *Vs* in D″ assuming that *Vs* varies linearly from the AK135 value at 2,591 km depth to $V_{CMB}$ at the CMB. We define $V_{CMB}$ by *dVs*, which is the perturbation from the AK135 velocity, $V^0_{CMB}$, at the CMB. Hence, $V_{CMB} = (1 + dVs)\, V^0_{CMB}$.

We build a catalog of waveform synthetics for each of the eight earthquakes from Table S1, all stations of the CDSN, and 3-D models in which *dVs* varies from −5% to +5% with a step of 0.1%. We cross-correlate these waveforms with the waveforms for the 1-D reference model and determine *dVs* that reproduces $\delta t^{3D}$ for each

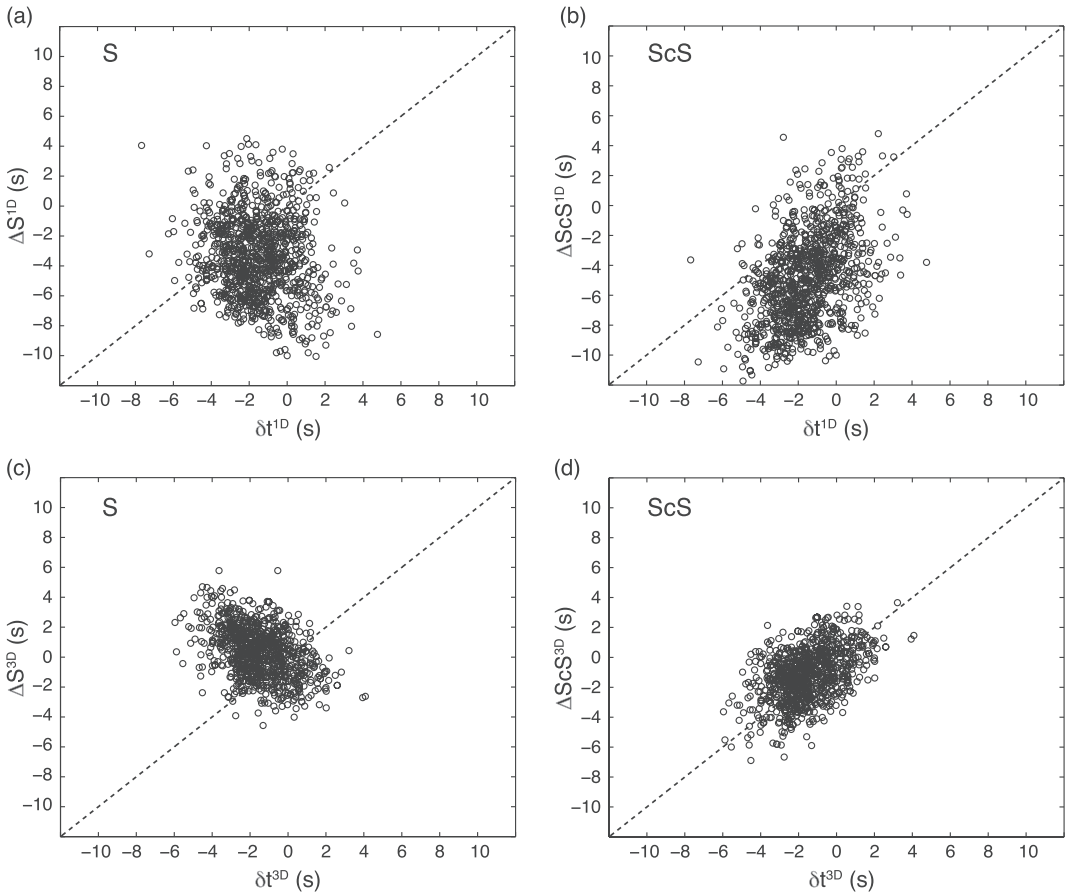


**Figure 3.** Comparison of the *ScS* and *S* arrival time anomalies. (a) $\Delta S^{1D}$ versus $\delta t^{1D}$, (b) $\Delta ScS^{1D}$ versus $\delta t^{1D}$, (c) $\Delta S^{3D}$ versus $\delta t^{3D}$, and (d) $\Delta ScS^{3D}$ versus $\delta t^{3D}$.

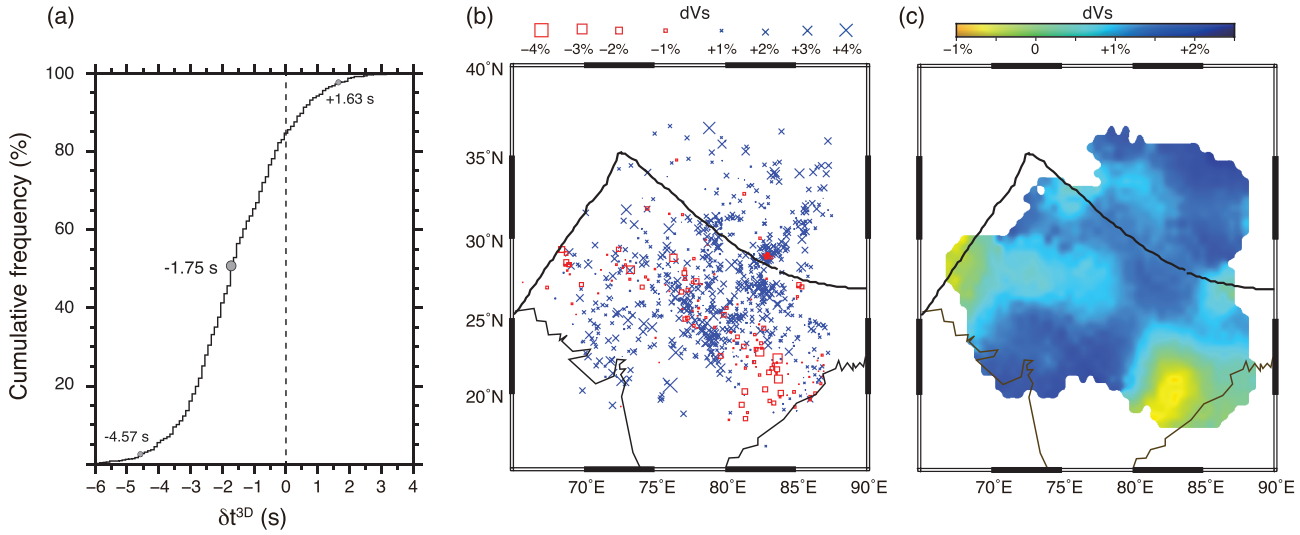


**Figure 4.** (a) Cumulative frequency histogram of $\delta t^{3D}$. The median value of $\delta t^{3D}$ is −1.75 s and 95% of the values fall between −4.57 s and +1.63 s. (b) Values of *dVs* plotted at the CMB reflection points of *ScS*. Blue crosses and red squares correspond to positive and negative values, respectively. The size of the symbols is proportional to the magnitude of *dVs*. (c) Map of *dVs* after cap smoothing using caps with radii of 2° and cap centers spaced every 0.5°. Each cap contains at least 10 values of *dVs*.

of the 929 source-receiver pairs. Because we assume that D″ is 300 km thick, we can only resolve the spatial variations of *dV*s associated with the variation of $\delta t^{3D}$. The range in *dV*s would be larger or smaller if we had chosen D″ to be thinner or thicker than 300 km, respectively.

Figure 4b shows a map of *dV*s plotted at the *ScS* reflection points. Overall, *dV*s is positive. The highest and lowest values of *dV*s are +4.2% and −2.8% and resolved in the central portion and near the southeastern margin of the reflection point region separated by less than 300 km. *ScS* reflection points associated with negative values for *dV*s are scattered throughout the central portion and form two coherent clusters in the southeastern and westernmost parts of the sampling region, roughly coincident with patches of relative weak *Vs* perturbations in S40RTS (see Figure 1a).

We show the average values of *dV*s in Figure 4c. For each average value of *dV*s, the *ScS* reflections points fall within a circular cap with a radius of 2°. The cap centers form a 0.5° × 0.5° grid. After averaging, the total variation in *dV*s is reduced by about a factor of 4 to about −1% to +2% but, as in Figure 4b, *dV*s appears to be lower within the central portion and lowest in two patches in the southeastern and western parts of the sampling region.

The average values of *dV*s depend on the assumed cap radius (Figure S6). This indicates that our modeling of $\delta t^{3D}$ with 1-D profiles of *Vs* in D″ cannot fully capture the complexity of the data and the sampling of D″ by *ScS* along nonvertical paths. However, the relatively smooth spatial variation of *dV*s across the sampling region does not change when the cap radius is larger than 2°. In the smoothest maps, *dV*s varies by at least 2% over less than 300 km in some parts of the sampling region. These gradients are much stronger than the gradients resolved by S40RTS and other tomographic models.

## 4. Discussion and Conclusions

Based on the modeling of waveforms of the phases *S* and *ScS* produced by earthquakes along the Owen Fracture Zone and beneath the Red Sea and recorded at stations from the Chinese Digital Seismic Network, we constrain *ScS*-S travel time (i.e., $\delta t$) variations and the 100-km scale *Vs* structure within a 2,000 × 2,000 $km^2$ zone of D″ beneath northern India, Nepal, and southwestern China near the plate boundary of the Neo-Tethys slab. As expected for a region modified by subduction since the Cretaceous and as imaged consistently by tomographic studies, we find that *Vs* is high compared to standard seismic profiles for the lowermost mantle. However, the variation of $\delta t$ by more than 6 s indicates that horizontal variations of *Vs* are stronger than can be resolved by seismic tomography.

It is widely recognized that the complex seismic structure implies that D″ is thermochemical boundary layer, possibly with distributed partial melts and anisotropy (e.g., Lay et al., 2004). The proposed scenarios by which the heterogeneity is formed are diverse. The seismic heterogeneity may be explained by material left-over after Earth's differentiation (e.g., Labrosse et al., 2007; Lee et al., 2010), chemical reactions between the mantle and core (e.g., Dubrovinsky et al., 2003), basalt-harzburgite segregation within the subducted slab that has reached the CMB (e.g., Andrault et al., 2014; Pradhan et al., 2015; Tackley, 2011), enrichment of Fe and Al in postperovskite (Mao et al., 2014), or with thermal anomalies that may point to incipient plume formation (He et al., 2014).

In the southeastern part of our sampling region, where data coverage is relatively high, horizontal variations in *Vs* are the strongest. The strength of the horizontal *Vs* gradients is uncertain because spatial variability in $\delta t$ is high and the unilateral sampling of D″ for the predominantly southwest-northeast oriented source-receiver combinations necessitates a 1-D modeling of $\delta t$. We estimate that *Vs* changes by 3–7% over distances shorter than 300 km at the CMB, as strong as what has been observed near the margins of large low shear velocity provinces (e.g., Ford et al., 2006; Sun & Miller, 2013). This variation depends on the assumptions of the thickness of D″ and the level at which we average $\delta t$. The estimated variation of *Vs* is higher if they are more strongly concentrated at the CMB. In the extreme case that ultralow velocity zones are responsible for the variability in $\delta t$, their shear velocity reductions must be about 15–35% for thickness between 20 and 50 km in order to explain a variation of $\delta t$ of 4 s. We note that there is no evidence for pervasive ULVZs in the lowermost mantle beneath eastern Asia (e.g., Yu & Garnero, 2018). Our work cannot discriminate between geodynamic scenarios for the generation of thermochemical heterogeneity in D″ in

downwelling regions of the mantle but our seismic modeling indicates that successful models must explain shear-velocity gradients of 3–7% over distances as short as 300 km.

**Acknowledgments**
This research is supported by the National Natural Science Foundation of China (41761144076) and K. C. Wong Education Foundation (GJTD-2019-04) to L.B., the National Natural Science Foundation of China (41804083) and China Postdoctoral Science Foundation (2018M641490) to G.L., and the National Science Foundation (EAR-1644829) to J.R. The CDSN waveforms were provided to us by the Data Management Center of the China National Seismic Network at the Institute of Geophysics, China Earthquake Administration (SEISDMC; doi:10.11998/seisdmc/SN). The data used to produce Figure 4 can be obtained from the National Tibetan Plateau Data Center (https://data.tpdc.ac.cn/en/data/ae2956b7-c44f-44f7--be13-436b83b60777). Some calculations were done on the Sherlock cluster at the Department of Geophysics, Stanford University. GMT software (Wessel & Smith, 1998) was used to prepare some of the figures. We thank the editor and two anonymous reviewers for their constructive comments.

## References

Andrault, D., Pesce, G., Bouhifd, M. A., Bolfan-Casanova, N., Hénot, J. M., & Mezouar, M. (2014). Melting of subducted basalt at the core-mantle boundary. *Science*, *344*(6186), 892–895. http://doi.org/10.1126/science.1250466

Bai, L., Li, G., Khan, N. G., Zhao, J., & Ding, L. (2017). Focal depths and mechanisms of shallow earthquakes in the Himalayan-Tibetan region. *Gondwana Research*, *41*, 390–399. http://doi.org/10.1016/j.gr.2015.07.009

Dubrovinsky, L., Dubrovinskaia, N., Langenhorst, F., Dobson, D., Rubie, D., Geßmann, C., et al. (2003). Iron-silica interaction at extreme conditions and the electrically conducting layer at the base of Earth's mantle. *Nature*, *422*(6927), 58–61. https://doi.org/10.1038/nature01422

Ford, S. R., Garnero, E. J., & McNamara, A. K. (2006). A strong lateral shear velocity gradient and anisotropy heterogeneity in the lowermost mantle beneath the southern Pacific. *Journal of Geophysical Research*, *111*, B03306. https://doi.org/10.1029/2004JB003574

Gaherty, J. B., & Lay, T. (1992). Investigation of laterally heterogeneous shear velocity structure in D″ beneath Eurasia. *Journal of Geophysical Research*, *97*, 417–435. https://doi.org/10.1029/91JB02347

Garnero, E. J., & Lay, T. (2003). D″ shear velocity heterogeneity, anisotropy and discontinuity structure beneath the Caribbean and Central America. *Physics of the Earth and Planetary Interiors*, *140*, 219–242. http://doi.org/10.1016/j.pepi.2003.07.014

Grocholski, B., Catalli, K., Shim, S.-H., & Prakapenka, V. (2012). Mineralogical effects on the detectability of the postperovskite boundary. *Proceedings of the National Academy of Sciences of the United States of America*, *109*(7), 2275–2279. http://doi.org/10.1073/pnas.1109204109

He, Y., & Wen, L. (2011). Seismic velocity structures and detailed features of the D″ discontinuity near the core-mantle boundary beneath eastern Eurasia. *Physics of the Earth and Planetary Interiors*, *189*(3–4), 176–184. http://doi.org/10.1016/j.pepi.2011.09.002

He, Y., Wen, L., Capdeville, Y., & Zhao, L. (2015). Seismic evidence for an Iceland thermo-chemical plume in the Earth's lowermost mantle. *Earth and Planetary Science Letters*, *417*, 19–27. https://doi.org/10.1016/j.epsl.2015.02.028

He, Y., Wen, L., & Zheng, T. (2014). Seismic evidence for an 850 km thick low-velocity structure in the Earth's lowermost mantle beneath Kamchatka. *Geophysical Research Letters*, *41*, 7073–7079. http://doi.org/10.1002/2014GL061249

Honza, E., & Fujioka, K. (2004). Formation of arcs and back-arc basins inferred from the tectonic evolution of Southeast Asia since the Late Cretaceous. *Tectonophysics*, *384*(1–4), 23–53. http://doi.org/10.1016/j.tecto.2004.02.006

Houser, C., Masters, G., Shearer, P., & Laske, G. (2008). Shear and compressional velocity models of the mantle from cluster analysis of long-period waveforms. *Geophysical Journal International*, *174*(1), 195–212. http://doi.org/10.1111/j.1365-246X.2008.03763.x

Kennett, B. L. N., Engdahl, E. R., & Buland, R. (1995). Constraints on seismic velocities in the Earth from traveltimes. *Geophysical Journal International*, *122*(1), 108–124. http://doi.org/10.1111/j.1365-246X.1995.tb03540.x

Kikuchi, M., & Kanamori, H. (1986). Inversion of complex body waves-II. *Physics of the Earth and Planetary Interiors*, *43*(3), 205–222. https://doi.org/10.1016/0031-9201(86)90048-8

Komatitsch, D., & Tromp, J. (2002). Spectral-element simulations of global seismic wave propagation—I. Validation. *Geophysical Journal International*, *149*(2), 390–412. http://doi.org/10.1046/j.1365-246X.2002.01653.x

Kustowski, B., Ekstrom, G., & Dziewonski, A. M. (2008). Anisotropic shear-wave velocity structure of the Earth's mantle: A global model. *Journal of Geophysical Research*, *113*, B06306. https://doi.org/10.1029/2007JB005169

Labrosse, S., Hernlund, J. W., & Coltice, N. (2007). A crystallizing dense magma ocean at the base of the Earth's mantle. *Nature*, *450*, 866–869. https://doi.org/10.1038/nature06355

Lay, T., Garnero, E. J., & Williams, Q. (2004). Partial melting in a thermo-chemical boundary layer at the base of the mantle. *Physics of the Earth and Planetary Interiors*, *146*, 441–467. https://doi.org/10.1016/j.pepi.2004.04.004

Lee, C. T. A., Luffi, P., Höink, T., Li, J., Dasgupta, R., & Hernlund, J. (2010). Upside-down differentiation and generation of a 'primordial' lower mantle. *Nature*, *463*, 930–933. https://doi.org/10.1038/nature08824

Mao, Z., Lin, J. F., Yang, J., Bian, H., Liu, J., Watsond, H. C., et al. (2014). (Fe,Al)-bearing post-perovskite in the Earth's lower mantle. *Earth and Planetary Science Letters*, *403*, 157–165. https://doi.org/10.1016/j.epsl.2014.06.042

Muller, R. D., & Seton, M. (2015). Paleophysiography of ocean basins. *Encyclopedia of Marine Geosciences.*. http://doi.org/10.1007/978-94-007-6644-0_84-1

Murakami, M., Hirose, K., Kawamura, K., Sata, N., & Ohishi, Y. (2004). Post-perovskite phase transition in $MgSiO_3$. *Science*, *304*(5672), 855–858. http://doi.org/10.1126/science.1095932

Pradhan, G. K., Fiquet, G., Siebert, F., Auzende, A., Morard, G., Antonangeli, D., & Garbarino, G. (2015). Melting of MORB at core–mantle boundary. *Earth and Planetary Science Letters*, *431*, 247–255. https://doi.org/10.1016/j.epsl.2015.09.034

Ricard, Y., Richards, M., & Le Stunff, Y. A. (1993). A geodynamical model of mantle density heterogeneity. *Journal of Geophysical Research*, *98*, 21,895–21,909. https://doi.org/10.1029/93JB02216

Ritsema, J. (2000). Evidence for shear velocity anisotropy in the lowermost mantle beneath the Indian Ocean. *Geophysical Research Letters*, *27*, 1041–1044. https://doi.org/10.1029/1999GL011037

Ritsema, J., Deuss, A., van Heijst, H. J., & Woodhouse, J. H. (2011). S40RTS: A degree-40 shear-velocity model for the mantle from new Rayleigh wave dispersion, teleseismic traveltime and normal-mode splitting function measurements. *Geophysical Journal International*, *184*, 1223–1236. https://doi.org/10.1111/j.1365-246X.2010.04884.x

Russell, S. A., Lay, T., & Garnero, E. J. (1998). Seismic evidence for small-scale dynamics in the lowermost mantle at the root of the Hawaiian hotspot. *Nature*, *396*(6708), 255–258. https://doi.org/10.1038/24364

Simmons, N. A., Forte, A., Boschi, L., & Grand, S. (2010). GyPSuM: A joint tomographic model of mantle density and seismic wave speeds. *Journal of Geophysical Research*, *115*, B12310. https://doi.org/10.1029/2010JB007631

Stampfli, G. M., & Borel, G. D. (2002). A plate tectonic model for the Paleozoic and Mesozoic constrained by dynamic plate boundaries and restored synthetic oceanic isochrones. *Earth and Planetary Science Letters*, *196*(1–2), 17–33. https://doi.org/10.1016/S0012-821X(01)00588-X.

Sun, D., & Miller, M. S. (2013). Study of the western edge of the African large low shear velocity province. *Geochemistry Geophysics Geosystems*, *14*, 3109–3125. https://doi.org/10.1002/ggge.20185

Tackley, P. J. (2011). Living dead slabs in 3-D: The dynamics of compositionally-stratified slabs entering a "slab graveyard" above the core-mantle boundary. *Physics of the Earth and Planetary Interiors*, *188*, 150–162. https://doi.org/10.1016/j.pepi.2011.04.013

Thomas, C., Wookey, J., & Simpson, M. (2007). D'' anisotropy beneath Southeast Asia. *Geophysical Research Letters*, *34*(4), L04301. https://doi.org/10.1029/2006GL028965

Thorne, M. S., & Garnero, E. J. (2004). Inferences on ultralow-velocity zone structure from a global analysis of *SPdKS* waves. *Journal of Geophysical Research*, *109*, B08301. https://doi.org/10.1029/2004JB003010

Van der Voo, R., Spakman, W., & Bijwaard, H. (1999). Tethyan subducted slabs under India. *Earth and Planetary Science Letters*, *171*(1), 7–20. https://doi.org/10.1016/S0012-821X(99)00131-4.

Weber, M., & Davis, J. P. (1990). Evidence of a laterally variable lower mantle structure from *P*- and *S*-waves. *Geophysical Journal International*, *102*, 231–255. https://doi.org/10.1111/j.1365-246X.1990.tb00544.x

Wessel, P., & Smith, W. H. F. (1998). New, improved version of the generic mapping tools released. *Eos. Trans. AGU*, *79*, 579.

Wysession, M. E., Fischer, K. M., Al-eqabi, G. I., Shore, P. J., & Gurari, I. (2001). Using MOMA broadband array, *ScS-S* data to image smaller-scale structures at the base of the mantle. *Geophysical Research Letters*, *28*(5), 867–870. https://doi.org/10.1029/2000GL008485

Young, C. J., & Lay, T. (1987). Evidence for a shear velocity discontinuity in the lower mantle beneath India and the Indian Ocean. *Physics of the Earth Planetary Interiors*, *49*, 37–53. https://doi.org/10.1016/0031-9201(87)90131-2

Yu, S., & Garnero, E. J. (2018). Ultralow velocity zone locations: A global assessment. *Geochemistry Geophysics Geosystems*, *19*, 396–414. https://doi. org/https://doi.org/10.1002/2017GC007281.

Zhang, B., Ni, S., & Sun, D. (2019). Seismological constraints on the small-scale heterogeneity in the lowermost mantle beneath East Asia and implication for its mineralogical origin. *Geophysical Research Letters*, *46*, 5225–5233. https://doi.org/10.1029/2019GL082296

Zhao, C., Garnero, E. J., Li, M., McNamara, A., & Yu, S. (2017). Intermittent and lateral varying ULVZ structure at the northeastern margin of the Pacific LLSVP. *Journal of Geophysical Research: Solid Earth*, *122*, 1198–1220. https://doi.org/10.1002/2016JB013449.

Zheng, X. F., Ouyang, B., Zhang, D. N., Yao, Z. X., Liang, J. H., & Zheng, J. (2009). Technical system construction of Data Backup Centre for China Seismograph Network and the data support to researches on the Wenchuan earthquake. *Chinese Journal of Geophysics (in Chinese)*, *52*(5), 1412–1417. https://doi.org/10.3969/j.issn.0001-5733.2009.05.031

## References From the Supporting Information

Chang, S. -J., Ferreira, A. M. G., Ritsema, J., van Heijst, H. J., & Woodhouse, J. H. (2015). Joint inversion for global isotropic and radially anisotropic mantle structure including crustal thickness perturbations. *Journal of Geophysical Research: Solid Earth*, *120*, 4278–4300. https://doi.org/10.1002/2014JB011824

Durand, S., Debayle, E., Ricard, Y., Zaroli, C., & Lambotte, S. (2017). Confirmation of a change in the global shear velocity pattern at around 1000 km depth. *Geophysical Journal International*, *211*(3), 1628–1639. https://doi.org/10.1093/gji/ggx405

Hosseini, K., Matthews, K. J., Sigloch, K., Shephard, G. E., Domeier, M., & Tsekhmistrenko, M. (2018). SubMachine: Web-based tools for exploring seismic tomography and other models of Earth's deep interior. *Geochemistry, Geophysics, Geosystems*, *19*, 1464–1483. https://doi.org/10.1029/2018GC007431

Koelemeijer, P., Ritsema, J., Deuss, A., & van Heijst, H. J. (2016). SP12RTS: A degree-12 model of shear- and compressional-wave velocity for Earth's mantle. *Geophysical Journal International*, *204*, 1024–1039. http://doi.org/10.1093/gji/ggv481

Lekić, V., & Romanowicz, B. (2011). Inferring upper-mantle structure by full waveform tomography with the spectral element method. *Geophysical Journal International*, *185*(2), 799–831. https://doi.org/10.1111/j.1365-246X.2011.04969.x

Lu, C., Grand, S. P., Lai, H., & Garnero, E. J. (2019). TX2019slab: A new *P* and *S* tomography model incorporating subducting slabs. *Journal of Geophysical Research: Solid Earth*, *124*, 11,549–11,567. https://doi.org/10.1029/2019JB017448

Moulik, P., & Ekstrom, G. (2014). An anisotropic shear velocity model of the Earth's mantle using normal modes, body waves, surface waves and long-period waveforms. *Geophysical Journal International*, *199*, 1713–1738. https://doi.org/10.1093/gji/ggu356

Panning, M. P., Lekić, V., & Romanowicz, B. A. (2010). Importance of crustal corrections in the development of a new global model of radial anisotropy. *Journal of Geophysical Research*, *115*, B12325. https://doi.org/10.1029/2010JB007520